

**AD-A255 860**

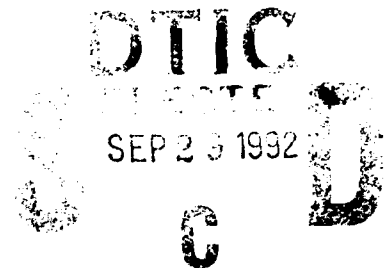


(2)

**NASA Contractor Report 189695**

**ICASE Report No. 92-40**

# ICASE



## **NUMERICAL STUDY OF THE SMALL SCALE STRUCTURES IN BOUSSINESQ CONVECTION**

**Weinan E  
Chi-Wang Shu**

Contract Nos. NAS1-18605 and NAS1-19480  
August 1992

Institute for Computer Applications in Science and Engineering  
NASA Langley Research Center  
Hampton, Virginia 23665-5225

Operated by the Universities Space Research Association

# NASA

National Aeronautics and  
Space Administration

Langley Research Center  
Hampton, Virginia 23665-5225

92 9 28 092

440183

**92-26066**



4088

# NUMERICAL STUDY OF THE SMALL SCALE STRUCTURES IN BOUSSINESQ CONVECTION

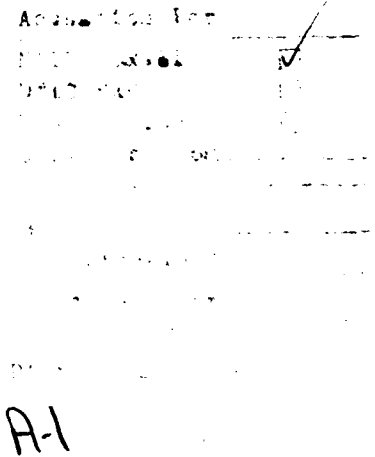
*Weinan E*<sup>1</sup>

School of Mathematics  
Institute for Advanced Study  
Princeton, New Jersey 08540

and

*Chi-Wang Shu*<sup>2</sup>

Division of Applied Mathematics  
Brown University  
Providence, Rhode Island 02912



## ABSTRACT

DTIC QUALITY INSPECTED 8

Two-dimensional Boussinesq convection is studied numerically using two different methods: a filtered pseudospectral method and a high order accurate ENO scheme. The issue whether finite time singularity occurs for initially smooth flows is investigated. The numerical results suggest that the collapse of the bubble cap reported by Pumir and Siggia is unlikely to occur in resolved calculations. The strain rate corresponding to the intensification of the density gradient across the front saturates at the bubble cap. We also found that the cascade of energy to small scales is dominated by the formation of thin and sharp fronts across which density jumps.

---

<sup>1</sup>The work of the first author was supported by ARO contract DAAL03-89-K-0039, AFOSR-90-0090, and NSF grant DMS-9100383.

<sup>2</sup>This research was supported by the National Aeronautics and Space Administration under NASA Contract Nos. NAS1-18605 and NAS1-19480 while the second author was in residence at the Institute for Computer Applications in Science and Engineering (ICASE), NASA Langley Research Center, Hampton, VA 23665. Research was also supported by ARO grant DAAL03-91-G-0123 and NASA Grant NAG1-1145.

## §1. Introduction

In this paper, we present the results of a careful and detailed numerical study of the small scale structures in two-dimensional Boussinesq convection in the absence of viscous effects. In particular, we address the issue of whether a finite time singularity can form from a smooth initial data. Recently in their numerical study of the same problem<sup>[14]</sup>, Pumir and Siggia observed that the cap of a symmetric rising bubble (with smooth density variation) collapses in a finite time. In contrast with their observations, our results suggest that such collapse cannot occur in a finite time. The strain rate associated with the intensification of the density gradient saturates, implying an exponential decay for the thickness of the front. This is reminiscent of the situation found in vortex reconnection<sup>[1,13,15]</sup>: when two vortex tubes are brought together, the axial strain rate saturates and the core of the tubes undergoes enormous deformation to avoid reconnection (in the absence of viscosity). Thus the inviscid solution manages to escape from forming a finite time singularity.

There are two main motivations for the study of the two-dimensional Boussinesq convection. One comes from the potential relevance of this problem to the study of atmospheric and oceanographic turbulence, as well as other astrophysical situations where rotation and stratification play a dominant role. The second motivation comes from the fact that from a computational viewpoint, this is the simplest among the class of incompressible flows which exhibit vorticity intensification. In particular, it is an open question whether the baroclinic generation of vorticity leads to a finite time singularity. Such singularities, if exist, provide an effective mechanism for the cascade of energy to small scales. This scenario also provides a convenient basis for various turbulence theories which assume, in one form or another, that the (ensemble average of) rate of viscous dissipation of energy remains finite in the limit of vanishing viscosity, implying the occurrence of finite time singularities in many Euler flows<sup>[12]</sup>.

There is a well-known analogy between the two-dimensional Boussinesq convection and the three-dimensional axisymmetric swirling flows:

$$(1.1) \quad \begin{cases} v_t + u v_r + w v_z + \frac{1}{r} u v = 0 \\ \omega_t + u \omega_r + w \omega_z - \frac{1}{r} u \omega - \frac{1}{r} (v^2)_z = 0 \end{cases}$$

Here  $\mathbf{u} = u \mathbf{e}_r + v \mathbf{e}_\theta + w \mathbf{e}_z$  is the velocity,  $\omega = u_z - w_r$  is the azimuthal vorticity. Comparing (1.1) with (2.1) – (2.4), we see that the centrifugal force plays a role similar to gravity, and the azimuthal circulation plays a role similar to density. Grauer and Sideris<sup>[9]</sup> were the first to seek finite time singularities in this restricted class. Although their numerical result still remains inconclusive, it has stimulated a lot of recent work along the same direction, including the present study.

A related problem was studied earlier by Childress<sup>[7]</sup> where he considered nearly two-dimensional Euler flows and derived effective equations governing their slow variation using contour averaging methods. Under a change of variables, the effective equation takes a form similar to the axisymmetric Euler equations with nonstandard connection between circulation, radius and the angular velocity component. Childress went further to study numerically a simplified version of his effective equations and observed finite time singularities for the simplified model. This was interpreted as a signal for the re-three-dimensionalization of the original (nearly two-dimensional) flow.

This paper is organized as follows. In §2. we formulate the problem and present some preliminary mathematical remarks. In §3. we describe the numerical methods used to study this problem. The numerical results are presented in §4. Some discussions and concluding remarks are made in §5.

## §2. Formulation of the Problem:

The equations describing Boussinesq convection are the following:

$$(2.1) \quad \begin{cases} \rho_t + \mathbf{u} \cdot \nabla \rho = 0 \\ \mathbf{u}_t + \mathbf{u} \cdot \nabla \mathbf{u} + \nabla p = - \begin{pmatrix} 0 \\ \rho \end{pmatrix} \\ \nabla \cdot \mathbf{u} = 0 \end{cases}$$

Here  $\rho$  is the density (this should be the temperature and denoted by  $\theta$  or  $T$ . But we are accustomed to calling it density, and therefore denote it by  $\rho$ ),  $\mathbf{u} = (u, v)$  is the velocity,  $p$  is the pressure. We have normalized the gravitational constant to be 1.

It is convenient to write (2.1) in the streamfunction – vorticity formulation:

$$(2.2) \quad \begin{cases} \rho_t + \mathbf{u} \cdot \nabla \rho = 0 \\ \omega_t + \mathbf{u} \cdot \nabla \omega = -\rho_x \\ -\Delta \psi = \omega \end{cases}$$

Here  $\omega$  is the vorticity,  $\psi$  is the stream function:

$$(2.3) \quad \omega = v_x - u_y \quad u = \psi_y, \quad v = -\psi_x.$$

Introducing the material derivative  $D_t = \partial_t + \mathbf{u} \cdot \nabla$ , (2.2) becomes simply

$$(2.4) \quad D_t \rho = 0, \quad D_t \omega = -\rho_x.$$

It is straightforward to show that if the initial data  $\mathbf{u}(x, y, 0) = \mathbf{u}_0(x, y)$  and  $\rho(x, y, 0) = \rho_0(x, y)$  are smooth enough, then the solution to (2.1) exists and remains smooth for a short time. It is not clear whether any solution would loss its regularity at a finite time. However, following Beale, Kato and Majda<sup>[3]</sup>, one can show that if a solution losses its regularity, then the density gradient has to blow up. More precisely, we have:

**Theorem:** *Define the norms:*

$$\|f(\cdot)\|_m = \left( \sum_{\substack{\alpha_1, \alpha_2 \geq 0 \\ \alpha_1 + \alpha_2 \leq m}} \int_{R^2} \left| \frac{\partial^{\alpha_1 + \alpha_2} f}{\partial x^{\alpha_1} \partial y^{\alpha_2}} \right|^2 dx dy \right)^{1/2}$$

$$|f(\cdot)|_\infty = \max_{(x, y) \in R^2} |f(x, y)|.$$

Assume that for some  $m > 2$ ,  $\|\mathbf{u}(\cdot, 0)\|_m + \|\rho(\cdot, 0)\|_m$  is finite, but there exists a  $T^*$  such that  $\|\mathbf{u}(\cdot, T^*)\|_m + \|\rho(\cdot, T^*)\|_m = +\infty$ . Then

$$(2.5) \quad \int_0^{T^*} |\omega(\cdot, t)|_\infty dt = +\infty$$

and

$$(2.6) \quad \int_0^{T^*} \int_0^t |\rho_x(\cdot, s)|_\infty ds dt = +\infty.$$

**Proof:** We will only give a sketch of the proof since it follows closely the argument of Beale, Kato and Majda<sup>[3]</sup>. We will use  $C$  to denote a generic constant.

Straightforward energy estimates lead to

$$\frac{d}{dt} \|\rho(\cdot, t)\|_m^2 \leq |\nabla \mathbf{u}(\cdot, t)|_\infty \|\rho(\cdot, t)\|_m^2,$$

$$\frac{d}{dt} \|\mathbf{u}(\cdot, t)\|_m^2 \leq |\nabla \mathbf{u}(\cdot, t)|_\infty \|\mathbf{u}(\cdot, t)\|_m^2 + \|\rho(\cdot, t)\|_m^2.$$

The logarithmic Sobolev inequality gives us, for  $m \geq 2$

$$|\nabla \mathbf{u}(\cdot, t)|_\infty \leq C |\omega(\cdot, t)|_\infty (1 + \log \|\mathbf{u}(\cdot, t)\|_m).$$

Therefore, if we let

$$y(t) = \|\rho(\cdot, t)\|_m^2 + \|\mathbf{u}(\cdot, t)\|_m^2,$$

we have

$$\dot{y}(t) \leq C |\omega(\cdot, t)|_\infty (1 + \log y(t)) y(t).$$

Solving this differential inequality, we get

$$y(t) \leq e^{e^C \int_0^t |\omega(\cdot, s)|_\infty ds} y(0).$$

On the other hand, since  $D_t \omega = -\rho_x$ , we have

$$\frac{d}{dt} |\omega(\cdot, t)|_\infty \leq |\rho_x(\cdot, t)|_\infty.$$

Hence

$$|\omega(\cdot, t)|_\infty \leq \int_0^t |\rho_x(\cdot, s)|_\infty ds + C$$

and

$$y(t) \leq e^{e^C \int_0^t \int_0^s |\rho_x(\cdot, t)|_\infty d\epsilon ds} y(0).$$

Since  $y(0)$  is finite, we conclude that if  $y(T^*) = +\infty$ , then (2.5) and (2.6) hold.

### §3. The Numerical Methods:

Computing singular or nearly singular solutions is a difficult task, particularly so in the context of incompressible flows. To obtain maximum information one has to push the

numerical method to the point where the flow is only marginally resolved. In this situation any numerical method is likely to exhibit its own artifact. Such numerical artifacts may not go away under simple mesh refinement checks, and they do not necessarily manifest themselves in scales comparable to the grid size. Therefore, there is a real danger of being misled by a particular numerical result. To avoid this, we have solved (2.1) using two different numerical methods: a Fourier - collocation method and an ENO scheme. When the solution develops large gradients, the Fourier - collocation method usually exaggerates the situation, whereas the ENO scheme tends to smear out the large gradients. By comparing the numerical results using the two different methods, we can better judge what phenomena is likely to be physical. Below we will describe separately the two methods.

### 3.1 Spectral Method with Smoothing

This is the standard Fourier-collocation method<sup>[6]</sup> with smoothing or de-aliasing. Roughly speaking, the differentiation operator is approximated in the Fourier space, while the nonlinear operations such as multiplications are done in the physical space. We used the intrinsic Cray FFT routines which considerably enhanced the performance of the code.

Since the solutions have large gradients, it is crucial to add filters to the spectral method in order that the numerical solutions do not degrade catastrophically if some part of the steep gradients are not adequately resolved. A robust way of adding the filters<sup>[20]</sup> is to replace the Fourier multiplier  $ik_j$  for the differentiation operator  $\partial_{x_j}$  by  $ik_j\varphi(|k_j|)$ , where

$$(3.1) \quad \varphi(k) = \epsilon^{-\alpha \left(\frac{k}{N}\right)^{m_f}}, \quad \text{for } |k| \leq N.$$

Here  $N$  is the numerical cutoff for the Fourier modes,  $m_f$  is the order of the filter, and  $\alpha$  is chosen so that  $\varphi(N) = \epsilon^{-\alpha} = \text{machine accuracy}$ . The machine accuracy on Cray-YMP with single precision is roughly  $10^{-14}$ . Denote by  $F$  and  $F^{-1}$  respectively the forward and backward Fourier transform operators, then the numerical derivative is evaluated as

$$(3.2) \quad D_N f = F^{-1}(ik\varphi(|k|))Ff.$$

The accuracy of such an approximation scheme depends on the parameter  $m_f$ . For smooth functions  $f(x)$ , we have

$$(3.3) \quad \|f'(x) - D_N f(x)\| = O(N^{-m_f})$$

We will denote the Fourier-collocation method with  $m_f$ -th order filter as SPmf. Unless otherwise stated, the results presented in § 4.2 were computed with  $m_f = 10$ .

### 3.2 The ENO Scheme

The ENO (Essentially Non-Oscillatory) scheme is used for the convection (spatial) part of the flow. We use ENO schemes based on point values and numerical fluxes, developed by Shu and Osher in [16], [17]; see also [18].

To apply ENO approximations, the equation is first written in a conservation form. For example the first equation in (2.2) is written as

$$\rho_t + (u\rho)_x + (v\rho)_y = 0 \quad (3.4)$$

The ENO operator is then applied to each of the conservative derivatives in a dimension-by-dimension fashion: when approximating  $(u\rho)_x$ ,  $y$  is fixed. Unlike the compressible flow, the incompressible flow equations are naturally written in characteristic form. Thus no expensive characteristic decomposition is needed. Upwinding can be simply determined by the signs of  $u$  and  $v$ .

We shall only briefly describe the approximation of a single derivative, say  $f_x$ . More details can be found in [16], [17], and [18].

The conservative approximation is of the form:

$$(f_x)_j \equiv \frac{1}{\Delta x} (\hat{f}_{j+\frac{1}{2}} - \hat{f}_{j-\frac{1}{2}}) \quad (3.5)$$

which, for  $r$ -th order ENO scheme, approximates the derivative to  $r$ -th order:

$$\frac{1}{\Delta x} (\hat{f}_{j+\frac{1}{2}} - \hat{f}_{j-\frac{1}{2}}) = f_x|_{x=x_{j+\frac{1}{2}}} + \mathcal{O}(\Delta x^r) \quad (3.6)$$



where the numerical flux  $\hat{f}_{j+\frac{1}{2}}$  is obtained by interpolating the point values of  $f$  on a stencil of  $r + 1$  consecutive grid points. The stencil is chosen inductively as follows. For  $r = 1$ , we choose the stencil to be  $[j-1, j]$  or  $[j, j+1]$  depending on the sign of  $u$ . For  $r > 1$ , left or right neighboring points are added to the stencil at the previous level  $r - 1$  according to the absolute value of the divided differences they each give. In most of our calculations, we used  $r = 3$ . We will denote this method by ENO3. Notice that the scheme is actually  $r + 1$ -th order in  $L_1$  norm. That is, the third order ENO scheme we use is actually fourth order accurate in the  $L_1$  norm.

The potential equation in (2.2) is solved with a fourth order central differencing (implemented in the Fourier space via FFT) plus a fourth order exponential filtering in the Fourier space described above. This guarantees fourth order accuracy and in most cases avoids instability. We are not sure whether ENO should or can be applied to this potential solver, since it is an elliptic equation with possibly a singular right-hand-side. Unlike the compressible case, some small oscillations can still be seen in the ENO solution, probably due to this potential solver.

For the temporal discretization, we used Runge-Kutta methods of various order designed in<sup>[17]</sup>. No major difference between the 3rd, 4th and 5th order methods were found in the numerical results. It seems to be a general fact that temporal accuracy is much less important than the spatial accuracy. We used the third order version most often since it only requires three auxiliary arrays, whereas the fourth order version requires five auxiliary arrays. We take initial data that is periodic with period  $D$  where  $D = [0, 2\pi] \times [0, 2\pi]$ . The results reported below were computed using CFL equal to 0.5. This is very much within the stability region of these methods.

We point out that our experience strongly favors the use of high order schemes because of their small dispersive errors. In a marginally resolved situation, even though the filtered spectral method does generate small oscillations near the front where the density

experiences a jump, the oscillations are effectively localized near the front. This is because the spurious numerical oscillations travel at roughly the right speed which is the speed of the front. The higher the order of the filter, the more accurate the propagation speed, the more localized the oscillations. Of course the Gibbs phenomena eventually prevails and the numerical result becomes noise.

## §4. Numerical Results

### 4.1 Formation of the front

We have numerically integrated (2.1) with a variety of initial data. The initial density is usually a perturbation of the uniform state, and the perturbations are localized in each period. The early time evolution of such flows is characterized by the formation of a front across which density varies sharply. As time evolves, the front gets increasingly sharper and the tail starts to roll up. Figures 1 – 3 present the time development of such events for the initial data

$$(4.1) \quad \begin{cases} \omega(x, y, 0) = 0 \\ \rho(x, y, 0) = 50\rho_1(x, y)\rho_2(x, y)(1 - \rho_1(x, y)) \end{cases}$$

where

$$\rho_1(x, y) = \begin{cases} \exp\left(1 - \frac{\pi^2}{\pi^2 - x^2 - (y - \pi)^2}\right) & \text{if } x^2 + (y - \pi)^2 \leq \pi^2 \\ 0 & \text{otherwise,} \end{cases}$$

$$\rho_2(x, y) = \begin{cases} \exp\left(1 - \frac{(1.95\pi)^2}{(1.95)^2 - (x - 2\pi)^2}\right), & \text{if } |x - 2\pi| < 1.95\pi \\ 0 & \text{otherwise} \end{cases}$$

Figure 1 is the density contour at  $t = 1.6$  computed using SP10 on a  $512^2$  grid. At this time, the flow looks roughly like a rising bubble. Figure 2 presents the same information at  $t = 2.5$ . By now the outer boundary of the bubble has become a sharp front. We notice that as the bubble rises, it leaves behind a long and thin filament of light fluid. This is a check on the amount of numerical diffusion present in the scheme. A low order method with numerical viscosity (needed to stabilize the front) will destroy the thin filament. In

Figure 3a and 3b we present respectively, the contours of density and vorticity at  $t = 2.9$ . Now the filament of light fluid is thinner and longer, and the trailing edge of the front has rolled up. From Figure 3b we see that most of the vorticity resides on the front, the rest of the flow domain has very little vorticity. This fact is more drastically displayed in Figure 4a and 4b where we plot respectively, the slice of  $\omega$  and  $\rho_x$  at  $y = \pi$ . Since  $\omega$  and  $-\rho_x$  have the same sign, from the vorticity equation (2.2) we see that the vorticity peaks will be increasingly and monotonically sharper. However, it appears that this mechanism of baroclinic vorticity generation only gives rise to an exponential growth of vorticity. We will come back to this point later.

To better appreciate the nearly singular behavior and the computational difficulties we face, we will show a few more plots for the profiles of the density and the velocity. Figure 5a displays the evolution of the density along the symmetry axis  $x = \pi$  at times  $t = 0.5, 1, 1.5, 2$  and  $2.5$ . It shows clearly the formation of a front, similar to the formation of shock fronts in the solutions of the *Burgers equation*. At  $t = 2.5$ , SP10 on the  $512^2$  grid is not resolving the flow and small numerical oscillations appear on the profile. However the numerical oscillations die out on the refined grid  $1024^2$ . The result of the latter calculation is superimposed in Figure 5a on the solution of the  $512^2$  grid. In Figure 5b and 5c we show the slices of  $\rho$  and  $v$  respectively, at  $y = \pi$ ,  $t = 2.5$ . From these graphs one might be tempted to conclude that jumps have occurred in  $\rho$  and cusps have occurred in  $v$ . However, a closer look suggests that the cusp-like behavior in  $v$  and the discontinuous behavior in  $\rho$  go away under refinement. In Figure 5d we compare the numerical results for  $v$  on the  $512^2$  and  $1024^2$  grids in the cusp-like regions. It is seen that on the  $1024^2$  grid the solution looks much less singular. Similar phenomena were observed for  $\rho$ .

These results, particularly Figure 2 and 3a motivate the following question: Is it possible that the solution losses its regularity at the same time at the entire front? For this to happen there are only two possibilities. One is that while  $v$  develops cusps,  $\rho$  stays

smooth across the front. This is ruled out by Theorem 1 since it dictates that  $\rho$  and  $\omega$  must become singular at the same time. The second possibility is that  $\rho$  develops jumps across the entire front. In this case it is necessary that fluids with intermediate densities are suddenly swept to the back of the bubble. Clearly this requires infinite velocity whereas all of our numerical results give velocities that are very well bounded.

Before ending this subsection, we present the comparison of the numerical results computed using the two different methods described in §3. Figure 6a and 6b display respectively, the time history of the maximum and minimum density computed using SP10 on  $256^2$ ,  $512^2$ , and  $1024^2$  grids and ENO3 on the  $512^2$  grid. These quantities should be conserved by the exact solutions. As expected, ENO does a much better job in avoiding overshoots and undershoots. Figure 6c compares the numerical results for  $\rho$  at  $y = \pi$ ,  $t = 2.5$ , computed using SP10 and ENO3 on  $512^2$  grid. The result of SP10 undershoots much more than the result of ENO3, although the latter also contains some small numerical oscillations. On the other hand, although not shown here, ENO is usually less accurate than the Fourier-collocation method and contains more numerical dissipation.

#### 4.2 Evolutions of the bubble cap and other aspects of the flow.

When the bubble rises, lighter fluid has larger acceleration and heavier fluid has smaller acceleration. This results in the formation of fronts. However, once the front is formed, the pressure gradient becomes important across the front. In fact, as is shown in Figures 7a and 7b, the formation of increasingly larger pressure gradients may reverse the initial picture. In Figures 7a and 7b, we plot the slice of  $-\rho_y$ ,  $p$ , and the acceleration  $-(\rho + p_y)$  along the symmetry axis  $x = \pi$  at two different times  $t = 0.5$  and  $t = 2$ . At  $t = 0.5$ , the acceleration  $-(\rho + p_y)$  decreases across the front, whereas at  $t = 2$  it increases across the front. (The density  $\rho$  always decreases across the front, see Figure 5a) This implies that the velocity difference between the fluid particles at the tip and the back of the front will not increase further after  $t = 2$ , assuming that the picture remains valid.

From another viewpoint, the fluid on the symmetry axis satisfies

$$(4.2) \quad \begin{cases} \rho_t + v\rho_y = 0 \\ u = 0 \\ v_t + vv_y = -(\rho + p_y). \end{cases}$$

Let  $\xi = \rho_y$ ,  $\eta = v_y$ . Then we have

$$(4.3) \quad \xi_t + v\xi_y = -\eta\xi.$$

The growth of  $\xi$  is controlled by the strain rate  $\eta$ . In Figure 8a we exhibit the time history of the maximum of  $|\eta|$ . During the time interval displayed, the maximum of  $|\eta|$  always occurs at the bubble cap. The results of several different calculations agree remarkably well; the strain rate  $\eta$  saturates at about  $t = 1.7$ . Consequently, the maximum of  $|\xi|$  can at most grow exponentially. This is indeed so, as can be seen from Figure 8b. Other quantities, such as  $\omega$  and  $\rho_x$ , also grow at an exponential rate.

We have also done calculations with other sets of data. Here we will briefly report the results of a few cases.

Figures 9a -- 9c display the results for initial data

$$\begin{aligned} \omega(x, y, 0) &= 0 \\ \rho(x, y, 0) = \rho_3(x, y) &= \begin{cases} (2\pi - x) e^{-\frac{(x-\pi)^2 + (y-\pi)^2}{2.5^2 - (x-\pi)^2 - (y-\pi)^2}} & \text{if } (x - \pi)^2 + (y - \pi)^2 < 2.5^2 \\ 0, & \text{otherwise.} \end{cases} \end{aligned}$$

The contour curves of  $\rho$  at  $t = 4.5$  and  $t = 5$  are shown respectively in Figures 9a and 9b, whereas Figure 9c shows the time history of the strain rate  $|\eta|$  at the bubble cap. We observe that the strain rate begins to saturate at  $t \approx 4.25$  and then increases quickly at  $t \approx 4.8$ . This corresponds to the time when a mushroom forms out of the bubble cap, and the front changes its global configuration. We see that eventually the strain rate saturates again at about  $t = 5.25$ . We expect that the strain rate at the cap will not increase unless the flow changes its geometry at the cap.

Figures 10a – 10c present the numerical results for a set of more complicated initial data. The data is designed so that at later times the bubble front will develop two bumps instead of one as in Figure 9b. Again the increase of the strain rate at the cap is accompanied by a change of the front configuration: after  $t = 3.5$ , the front is no longer convex (as it was before  $t = 3.5$ ). We were not able to carry this computation further to see the eventual saturation, since the side arms of the bubble become so thin that they cannot be resolved on a  $1024^2$  grid. It is not clear whether a pinch actually occurs at the side arms.

## §5. Discussions and Conclusions

Our numerical results strongly suggest that the collapse of the bubble cap observed by Pumir and Siggia<sup>[14]</sup> is unlikely to occur in a resolved calculation. The increase of the strain rate is always associated with a global change of the flow character. The contribution of the local strain tends to saturate. The global character of the flow is important. Consequently any numerical procedure which employs some sort of local approximation is open to serious suspicion. This includes the ones presented in<sup>[14]</sup>. However, we did not address the issue whether other types of singularities can occur.

Let us reiterate the argument presented in §4.2. Along the symmetry axis  $x = \pi$ , we have

$$(5.1) \quad \begin{cases} D_t \xi = -\eta \xi \\ D_t \eta = -(\rho_y + p_{yy}) - \eta^2 \end{cases}$$

where  $\xi = \rho_y$ ,  $\eta = v_y$  are both negative at the front. From (2.1) we also have

$$(5.2) \quad -\rho_y - \Delta p = u_x^2 + v_y^2 + 2u_y v_x.$$

On the symmetry axis, this reduces to

$$(5.3) \quad -\rho_y - p_{yy} = p_{xx} + 2\eta^2.$$

Therefore, we have

$$(5.4) \quad \begin{cases} D_t \xi = -\eta \xi \\ D_t \eta = p_{xx} + \eta^2. \end{cases}$$

As long as the front remains relatively smooth,  $p_{xx}$  is negligible compared to  $\eta^2$ . Consequently  $\xi$  and  $\eta$  will stay bounded. In fact since near the cap  $\rho_y \leq 0$ ,  $p_{yy} \leq 0$ , we obtain a necessary condition for collapse at the cap:

$$(5.5) \quad -2\eta^2 \leq p_{xx} \leq -\eta^2.$$

In particular, the front itself has to develop infinite curvature. This is consistent with the argument presented in section 5 of<sup>[14]</sup>.

The key difference between the computations reported in<sup>[14]</sup> and the computations reported here, is that in<sup>[14]</sup> a high frequency instability (with a scale that is comparable to the thickness of the front) is observed at the cap, whereas in all our resolved calculations we have not seen the manifestation of such an instability. Since the front is extremely thin, near the cap the situation resembles that of the Rayleigh-Taylor instability. Therefore a linear stability theory will indeed predict that the front is unstable to short wavelength perturbations. However, the relevant question here is not whether perturbations can grow, but whether short wavelength perturbations can exist in a dynamic context. In other words, the issue is whether the exact solutions of (2.1) can supply perturbations with wavelength on the scale of the thickness of the front.

We want to emphasize that the question we are asking is a rather academic one. In actual physical experiments, various external noises provide ample sources of such perturbations. The solution we are seeking numerically may hardly occur in experiments. (This is yet another argument for the importance of scientific computing: It has the potential to carry out much more controlled experiments.)

Before discussing the question raised above, let us recall two problems that bear some similarity with the case we are studying. The first is the classical Kelvin-Helmholtz

instability of a vortex sheet. The braid that connects two consecutive rolls in a Kelvin-Helmholtz roll-up is still subject to Kelvin-Helmholtz instability, although the local vortex sheet strength is decreasing in time and the braid is under straining. This kind of instability manifests itself in numerical computations in such a way that the round-off error causes small spurious roll-ups along the braids. This phenomenon is studied very carefully by Krasny<sup>[11]</sup> and is cured by introducing a nonlinear filter that keeps the numerical solution effectively analytic.

The second problem is the behavior of an expanding bubble in a Hele-Shaw cell with very small surface tension. The presence of the surface tension makes the interface between two viscous fluids linearly stable. Nevertheless, the interface is nonlinearly unstable and prefers to develop the characteristic viscous fingers and the tip-splitting of these fingers observed in experiments. For example the amount of perturbation needed to upset the linear stability of a viscous finger and cause it to split is exponentially small in terms of the surface tension<sup>[4]</sup>. In the numerical studies of Dai and Shelley<sup>[8]</sup>, the lower precision calculations give rise to finger-like behavior. One might argue that such fingers are physical, on the basis that they are observed in experiments. But they are not faithful solutions of the original dynamic problem. Indeed as was shown by Dai and Shelley, the initial instability go away in the high precision calculations (128 bits).

Returning to the problem we are studying, the linear stability of the cap of a rising bubble is investigated by Batchelor et. al.<sup>[2,14]</sup>. In particular, Pumir and Siggia show that perturbations with wavelength  $\delta$  (the thickness of the front) can amplify by a factor of  $\frac{\gamma_c}{\delta}$  (where  $\gamma_c$  is the radius of curvature at the cap) if

$$(5.6) \quad \frac{\gamma_c}{\delta} \frac{1}{2\delta s^2} < e^{2((\frac{1}{2\delta s^2})^{1/2} - 1)}.$$

Here  $s$  is the strain rate at the cap. We remark that an infinitesimal disturbance eventually decays since the local strain increases its wavelength exponentially.



Although in some cases we have carried out the computation well beyond the limit set by (5.6), we have not observed the kind of instability at the cap reported by Pumir and Siggia<sup>[14]</sup>. One such instance is displayed in Figure 11 where we have roughly  $\delta = \frac{1}{256}$ ,  $\gamma_c = \frac{1}{4}$ ,  $s = 2$ . (5.6) becomes  $2048 < 1.109 \times 10^4$  and is very well satisfied. Still no instability on the front is observed.

A similar situation occurs in the classical Rayleigh-Taylor problem. The interface between a heavy fluid on top and a light fluid at the bottom is linearly unstable and typically evolves to mushroom-like or plume-like structures. The tips and tails of the structure are still subject to linear instability. But no instability at the tips or tails has been reported, even though the problem has been extensively studied<sup>[10,19]</sup>.

We remark that for the collapse to occur, a cascade of instabilities has to develop at the cap with increasingly smaller temporal and spatial scales. We have argued that such an instability is unlikely to arise for the true exact solutions of (2.1). However, since the front is very sensitive to numerical errors, any uncontrolled truncation can easily trigger the instability and lead to erroneous results.

With respect to the issue of formation of small scale structures, our calculation suggests that the cascade of energy to small scales is dominated by the formation of thin fronts. Roll-ups that are characteristic of two-dimensional Kelvin-Helmholtz instability also occur but play a less important role. Occasionally we also observe small rolls formed out of big rolls, evidence of what is suggested in Richardson's well-known quote. But these rolls carry a very small amount of energy. The scenario of a cascade through a sequence of roll-ups on increasingly smaller scales, if at all possible, has negligible contribution to the overall cascade mechanism.

The evolution of the energy spectrum for the first set of data is plotted in Figure 12. There is an apparent similarity to the spectrum observed by Brachet et. al. for the Taylor-Green vortex<sup>[5]</sup>. The near singular behavior creates an algebraically-decaying part

in the bulk of the spectrum. However the spectrum does not seem to settle down to any stationary state.

To conclude, let us emphasize that the ultimate answer to the question addressed here must be analytical. Numerical studies can at best provide partial evidence. For incompressible flows, it has proven very difficult to obtain analytical results on the regularity of the solutions. As a result, considerable efforts were devoted to the numerical approach. However, computing singular or nearly singular incompressible flows is also an extremely difficult task. Not surprisingly, the subject of seeking singularities numerically for incompressible flows is full of controversy. The contradicting conclusions reached in the present paper and the work of Pumir and Siggia<sup>[14]</sup> certainly adds one more to the list of many unsettled issues. It is our intention that these numerical work will generate sufficient interest for further analytical study and the evidence presented will contribute to the ultimate resolution of the issue raised.

#### **Acknowledgement:**

We are grateful to Steve Childress and Mike Shelley for numerous stimulating discussions. We also want to thank Eric Siggia for communicating his results to us. The numerical computation reported here was done on the Cray-YMP at the Pittsburgh Supercomputing Center.

## References

- [1] C. Anderson and C. Greengard, "The vortex ring merger problem at infinite Reynolds number". *Comm. Pure and Appl. Maths.*, xlii, p. 1123 (1989).
- [2] G.K. Batchelor, "The stability of a large gas bubble moving through a liquid". *J. Fluid Mech.*, 184, p. 399 (1987).
- [3] J.T. Beale, T. Kato and A. Majda, "Remarks on the breakdown of smooth solutions for the 3-D Euler equations". *Comm. Math Phys.*, 94, p. 61 (1984).
- [4] D. Bensimon, *Phys. Rev. A*, 33, 1302 (1986).
- [5] M. Brachet, D. Meiron, B. Nickel, S.A. Orszag and U. Frisch, "The small-scale structure of the Taylor-Green vortex". *J. Fluid Mech.*, 130, p. 411 (1983).
- [6] C. Canuto, M. Y. Hussaini, A. Quarteroni and T. A. Zang, "Spectral Methods in Fluid Dynamics". Springer-Verlag, New York, 1987.
- [7] S. Childress, "Nearly two-dimensional solutions of Euler's equations". *Phys. Fluids*, 30(4), p. 944 (1987).
- [8] Dai and M. Shelley, private communication.
- [9] R. Grauer and T. Sideris, "Numerical computation of 3D incompressible ideal fluids with swirl". *Phys. Rev. Letters*, 67, p. 3511 (1991).
- [10] R. M. Kerr, "Simulation of Rayleigh-Taylor flows using vortex blobs". *J. Comput. Phys.*, 76, p. 48 - 84 (1988).
- [11] R. Krasny, "Desingularization of periodic vortex sheet roll-up". *J. Comput. Phys.*, 65, p. 292 - 313 (1986).
- [12] A. Majda, "Vorticity, turbulence, and acoustics in fluid flow". *SIAM Review*, Vol. 33, No. 3, p. 349 - 388 (1991).
- [13] A. Pumir and E.D. Siggia, "Collapsing solutions to the 3D Euler equations". *Phys. Fluids A*, 2, p. 220 (1990).
- [14] A. Pumir and E.D. Siggia, "Development of singular solutions to the axisymmetric Euler equations". *Phys. Fluids A* - submitted.
- [15] M. J. Shelley, D. E. Meiron and S. A. Orszag, "Dynamical aspects of vortex reconnection of perturbed anti-parallel vortex tubes". *J. Fluid Mech.* - to appear.
- [16] C.-W. Shu and S. Osher, "Efficient implementation of essentially non-oscillatory shock capturing schemes." *J. Comput. Phys.*, v.77, 1988, pp.439-471.
- [17] C.-W. Shu and S. Osher, "Efficient implementation of essentially non-oscillatory shock capturing schemes, II." *J. Comput. Phys.*, v.83, 1989, pp.32-78.

- [18] C.-W. Shu, T.A. Zang, G. Erlebacher, D. Whitaker, and S. Osher, "*High order ENO schemes applied to two- and three- dimensional compressible flow.* " Appl. Numer. Math., v.9, 1992, pp.45-71.
- [19] G. Tryggvason, "*Numerical simulations of the Rayleigh-Taylor instability*". J. Comput. Phys. 75, p. 253 – 282 (1988).
- [20] H. Vandeven, "*Family of spectral filters for discontinuous problems*". J. Sci. Comput., v.6, pp. 159-192 (1991).

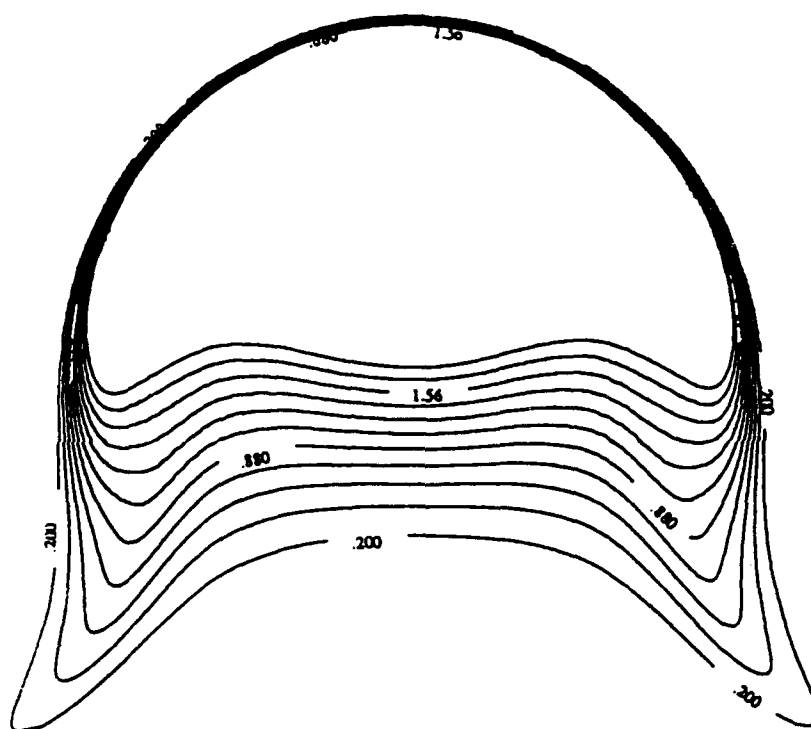


Figure 1. Density contour at  $t=1.6$  for initial data (4.1).

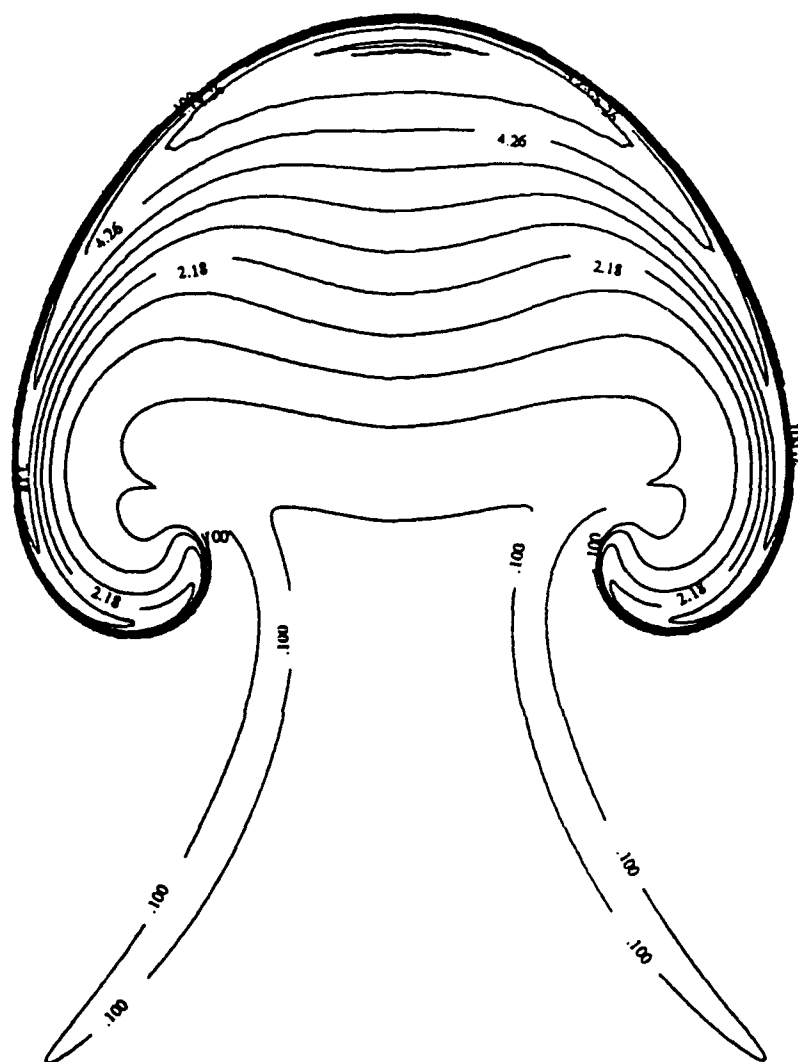


Figure 2. Density contour at  $t=2.5$  for initial data (4.1).

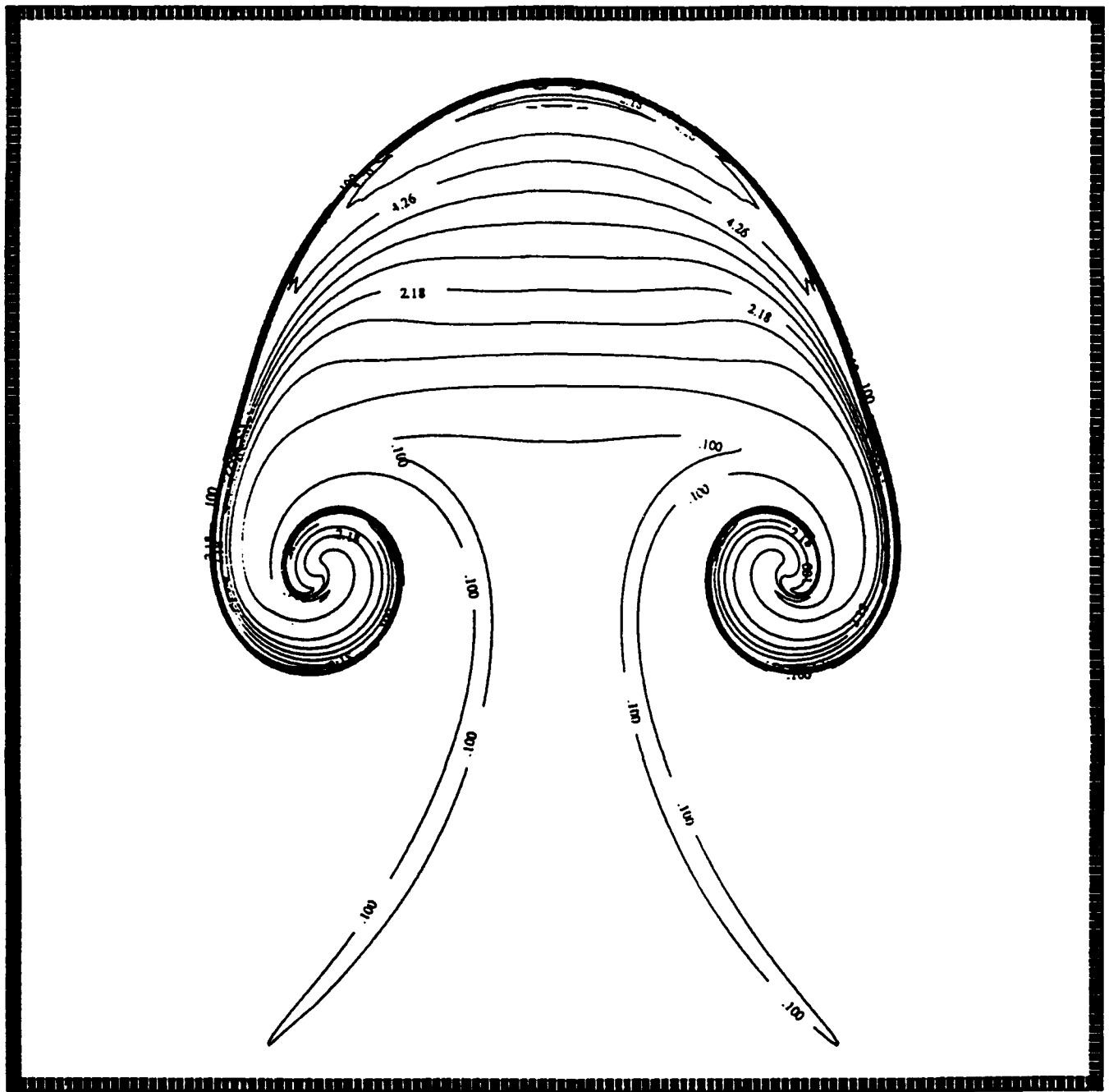


Figure 3a. Density contour at  $t=2.9$  for initial data (4.1).



Figure 3b. Vorticity contour at  $t=2.9$  for initial data (4.1).



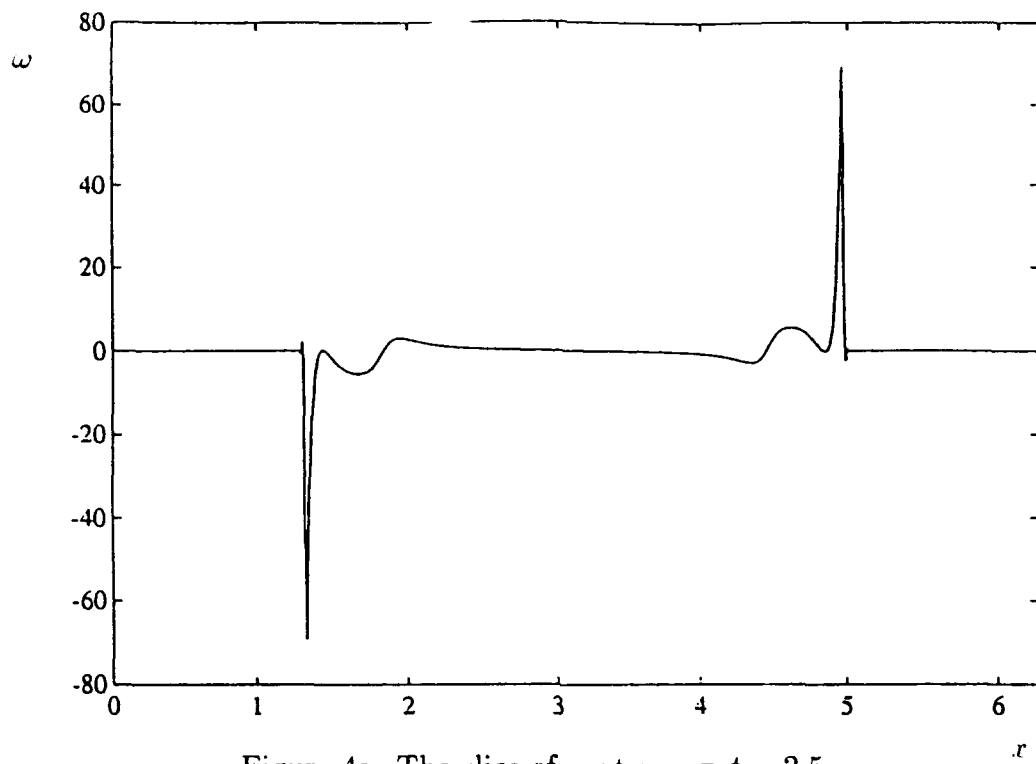


Figure 4a. The slice of  $\omega$  at  $y = \pi, t = 2.5$ .

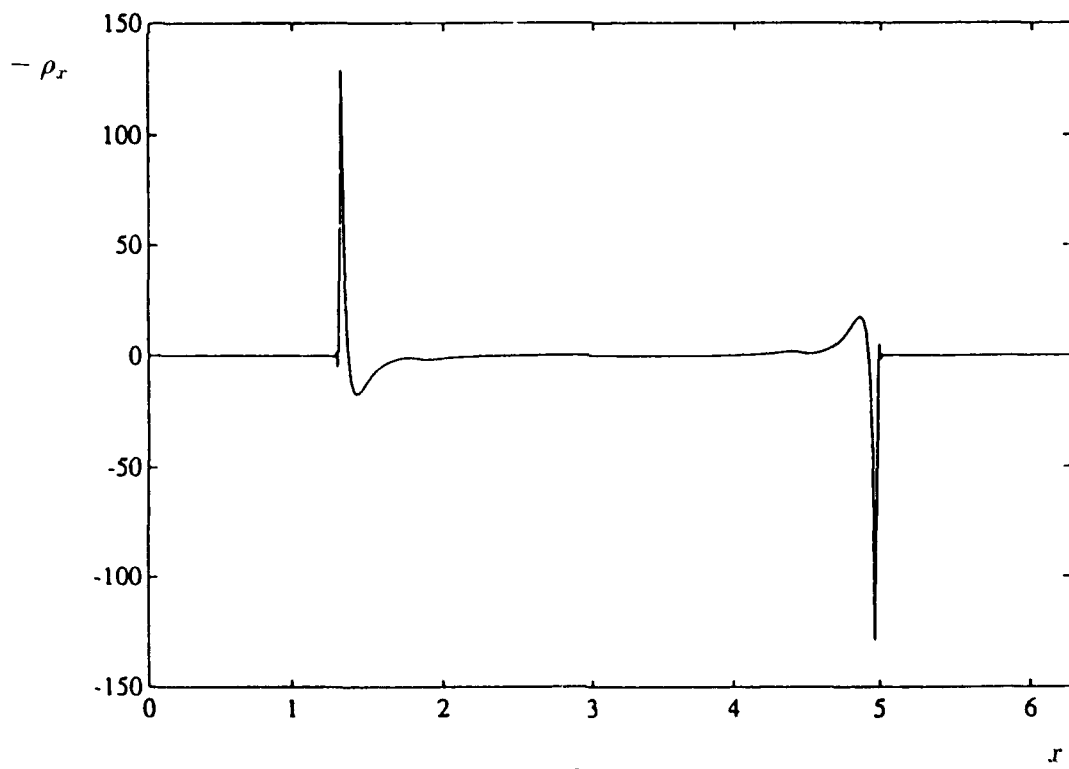


Figure 4b. The slice of  $-\rho_r$  at  $y = \pi, t = 2.5$ .

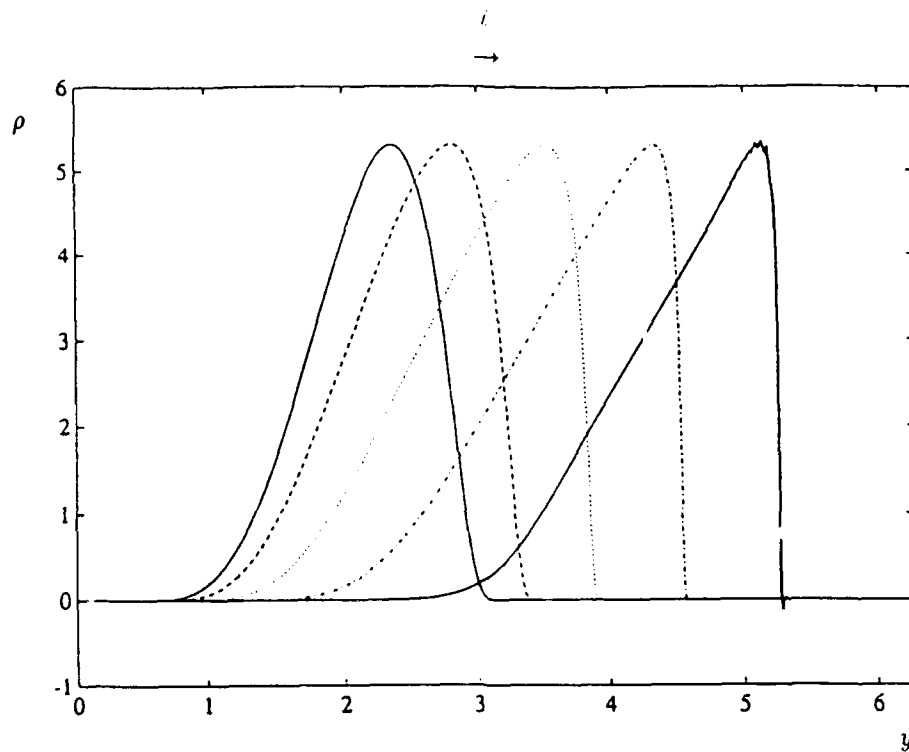


Figure 5a. Evolution of density along the symmetry axis  $x = \pi$  at  $t = 0.5, 1.0, 1.5, 2.0$  and  $2.5$ , computed using SP10 on a  $512^2$  grid. The result at  $t = 2.5$  computed on a  $1024^2$  grid is also superimposed. Notice that the small numerical oscillations disappear on the refined grid.

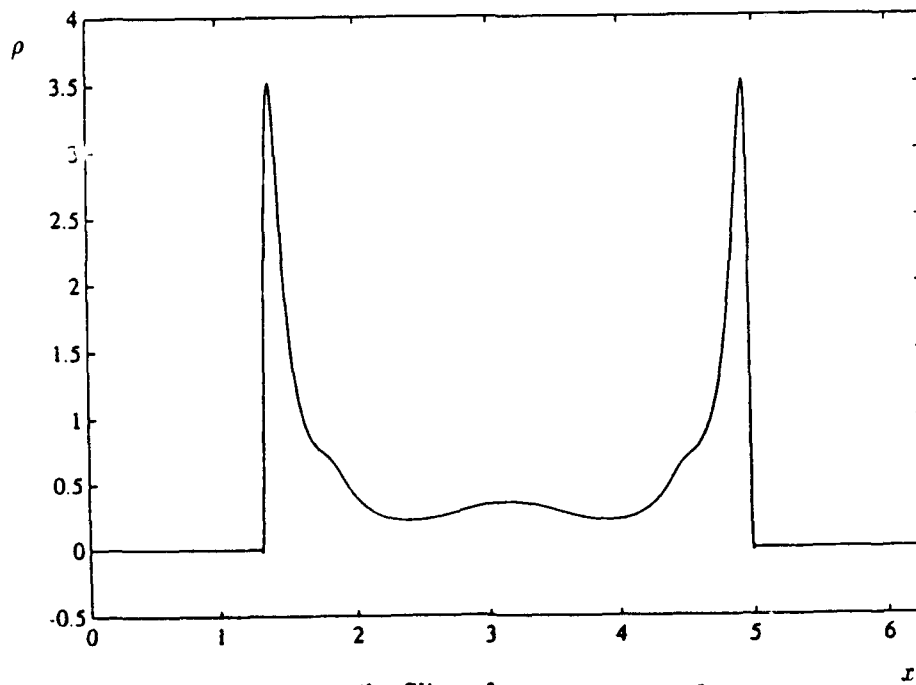


Figure 5b. Slice of  $\rho$  at  $y = \pi, t = 2.5$ .

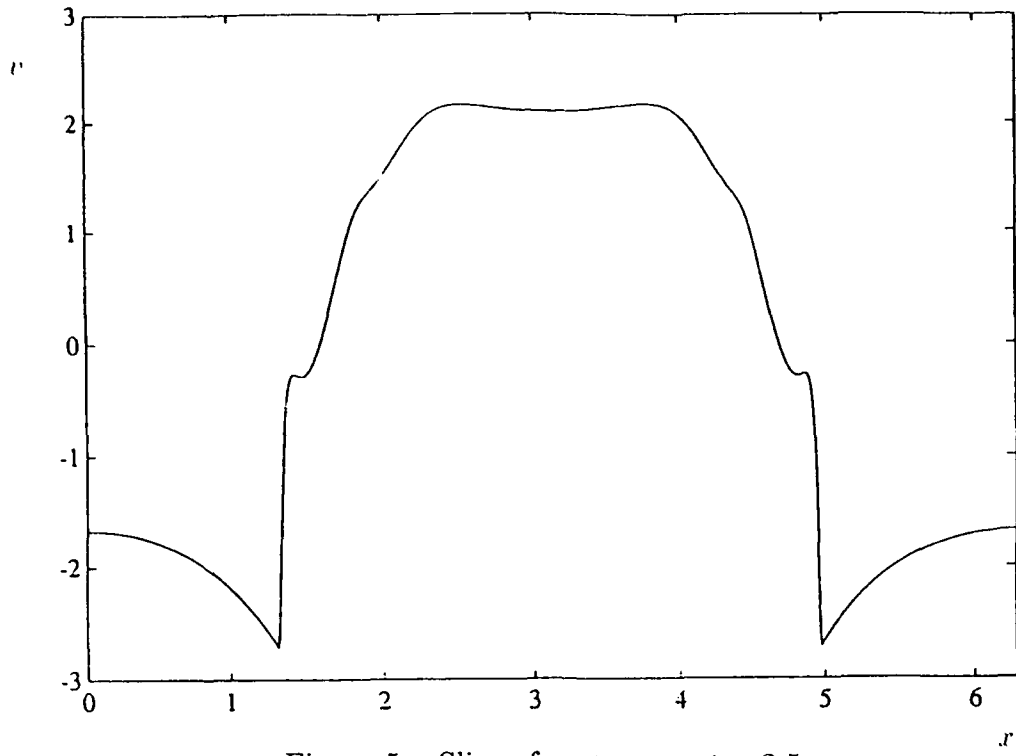


Figure 5c. Slice of  $v$  at  $y = \pi, t = 2.5$ .

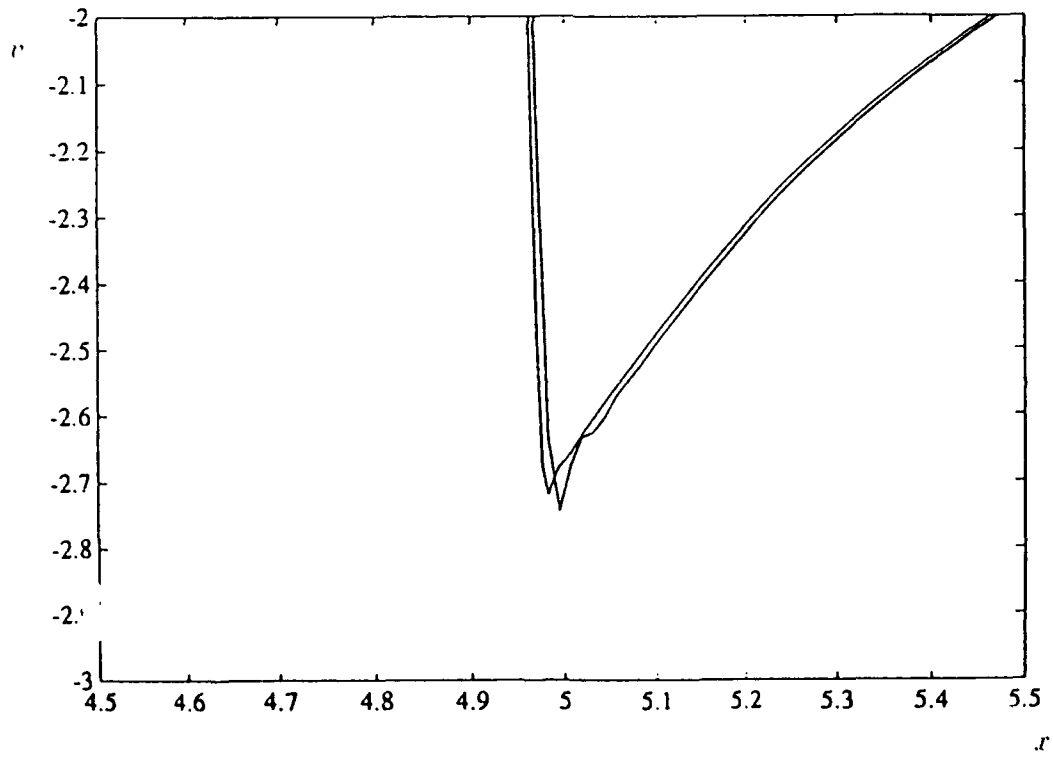


Figure 5d. Comparison of the numerical results of  $v$  in the cusp region for two different numerical resolutions:  $512^2$  and  $1024^2$ .

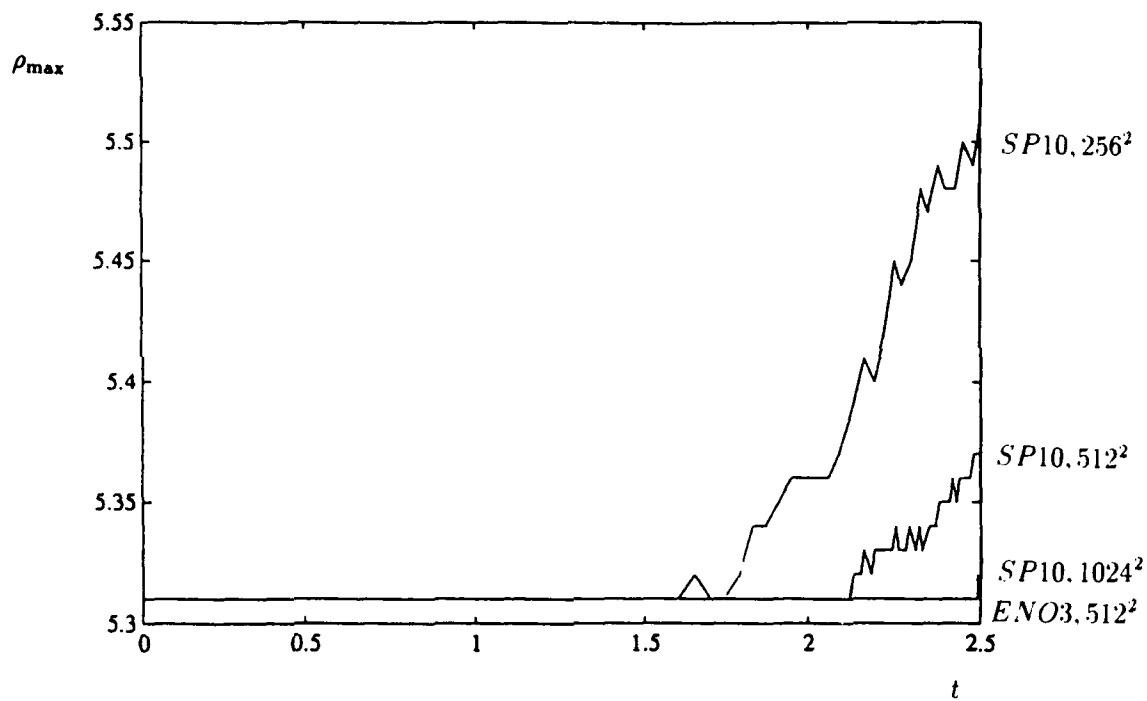


Figure 6a. Time history of the maximum density from different computations. From top to bottom: SP10 on the  $256^2$  grid, SP10 on the  $512^2$  grid, SP10 on the  $1024^2$  grid and ENO3 on the  $512^2$  grid.

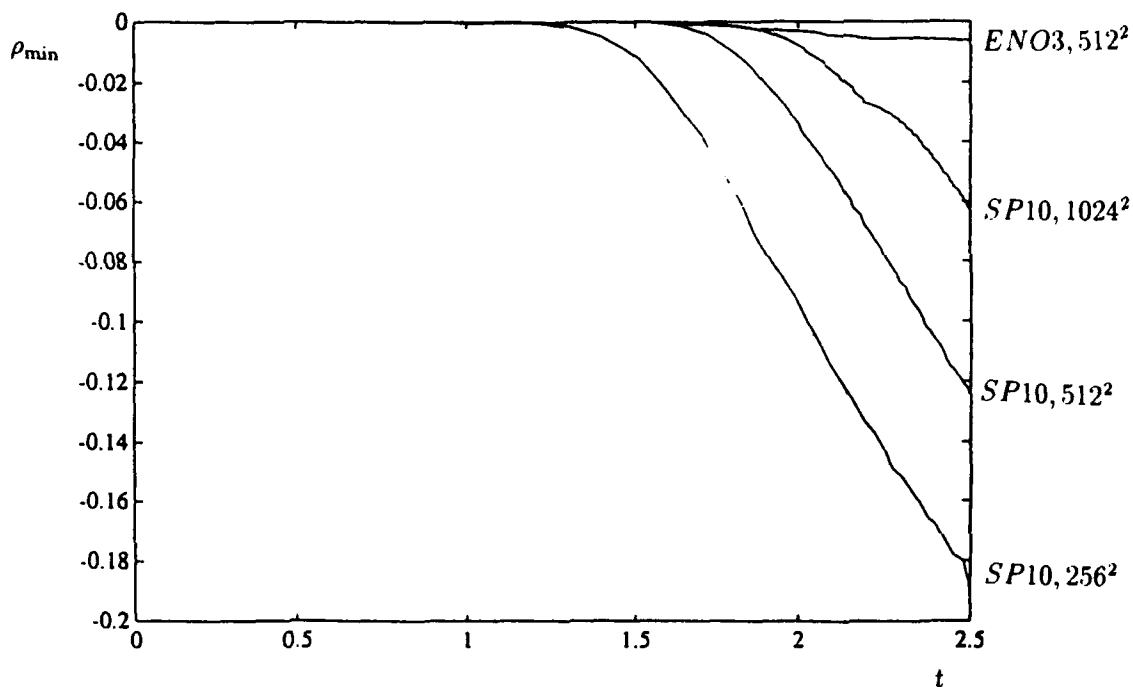


Figure 6b. Time history of the minimum density from different computations. From bottom to top: SP10 on the  $256^2$  grid, SP10 on the  $512^2$  grid, SP10 on the  $1024^2$  grid and ENO3 on the  $512^2$  grid.

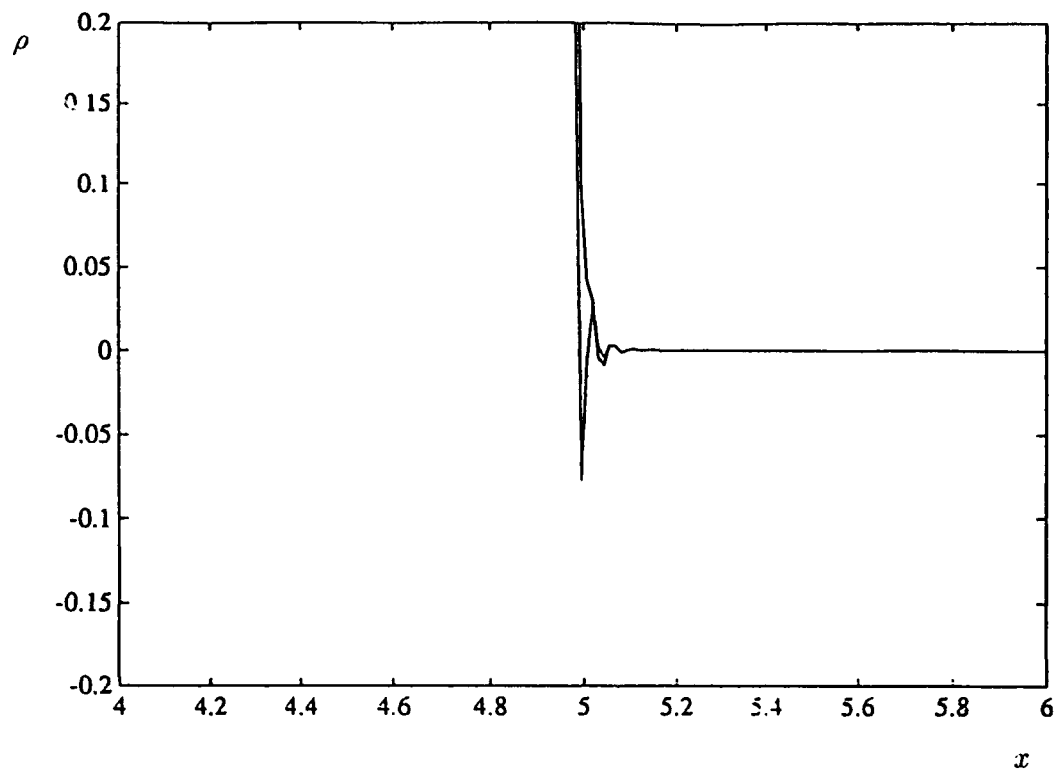


Figure 6c. Comparison of the numerical results for  $\rho$  across the front at  $y = \pi, t = 2.5$  for two different methods, SP10 and ENO3, both on the  $512^2$  grid. (See Fig. 5b for the full plot of SP10). ENO3 has less numerical oscillations.

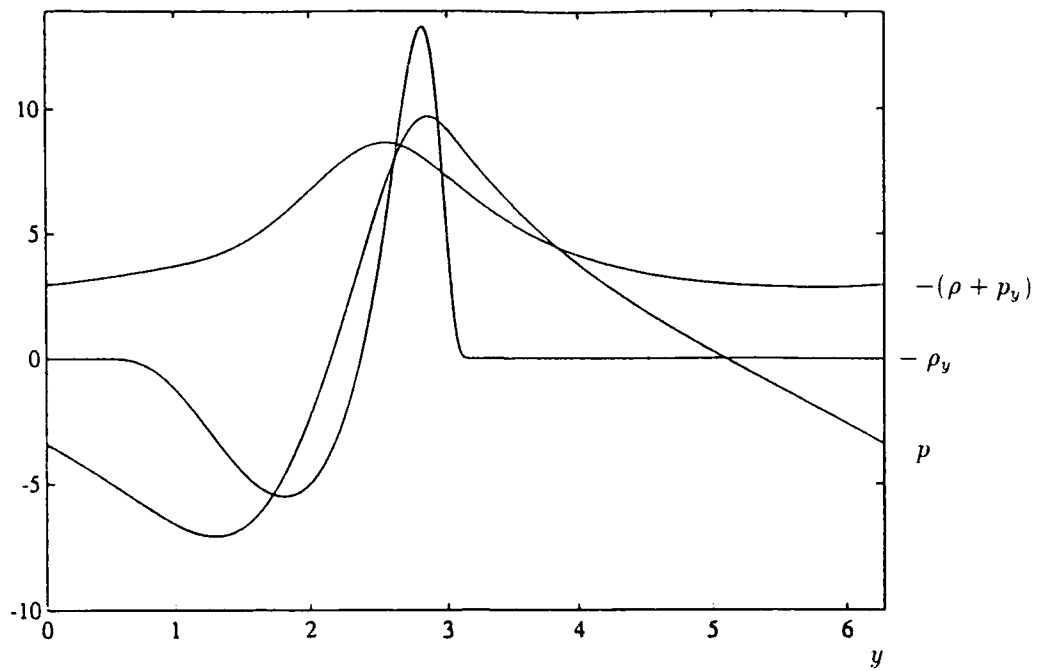


Figure 7a. Slice of  $-\rho_y$ ,  $p$  and  $-(\rho + p_y)$  at  $t = 0.5$  along the symmetry axis  $x = \pi$ . The acceleration  $-(\rho + p_y)$  decreases across the front.

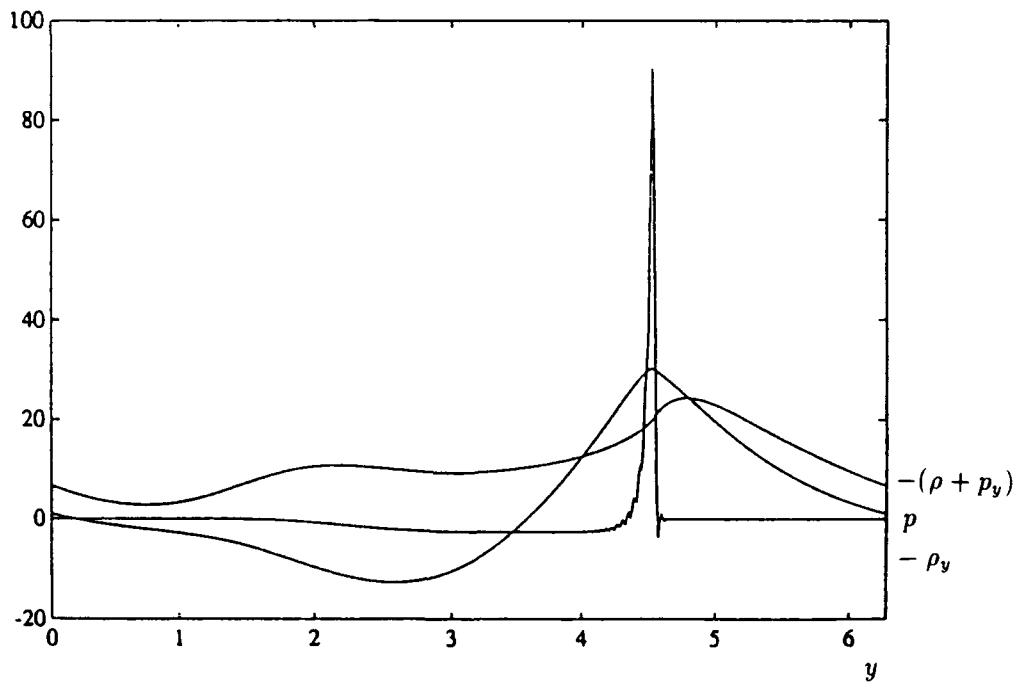


Figure 7b. Slice of  $-\rho_y$ ,  $p$  and  $-(\rho + p_y)$  at  $t = 2$  along the symmetry axis  $x = \pi$ . The acceleration  $-(\rho + p_y)$  now increases across the front.

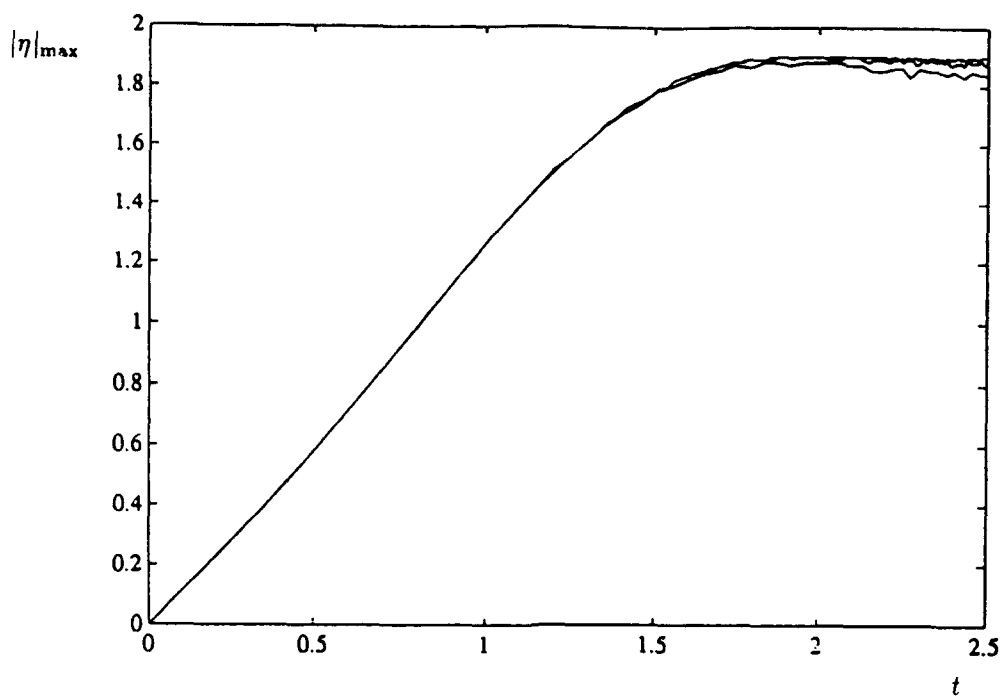


Figure 8a. Time history of the maximum of  $|\eta|$  at the front (which is also the strain rate  $v_y$  at the cap). From top to bottom: SP10 on  $1024^2$  grid, SP10 on  $512^2$  grid, and ENO3 on  $512^2$  grid. Strain rate saturates at  $t = 1.7$ .

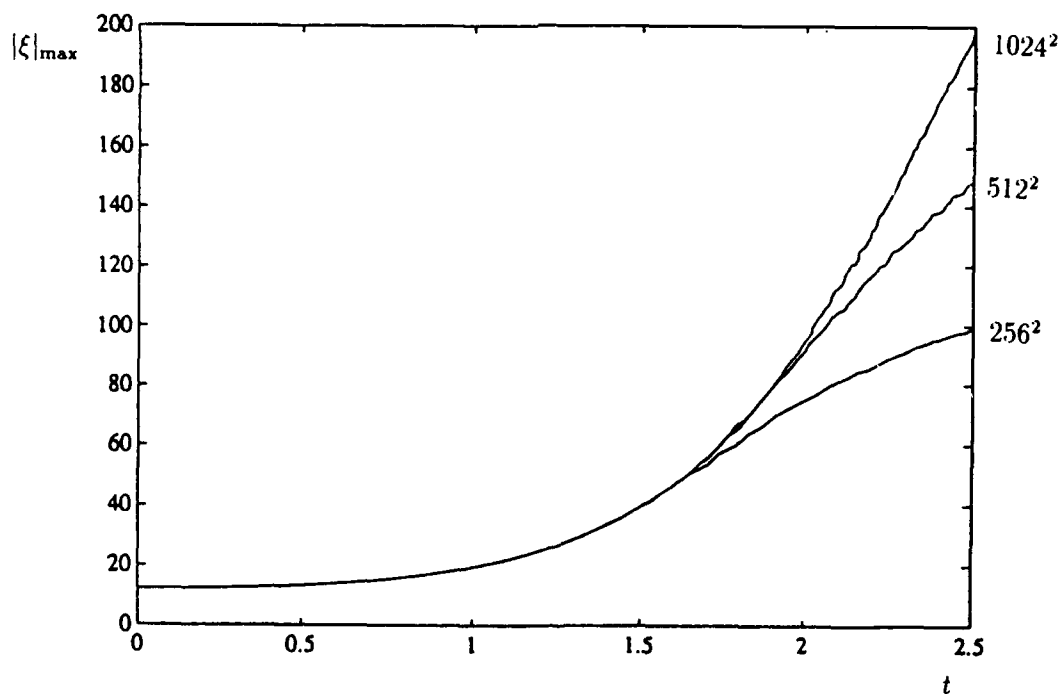


Figure 8b. Time history of the maximum of  $|\xi|$ . From top to bottom: SP10 on  $1024^2$  grid, SP10 on  $512^2$  grid, and SP10 on  $256^2$  grid.

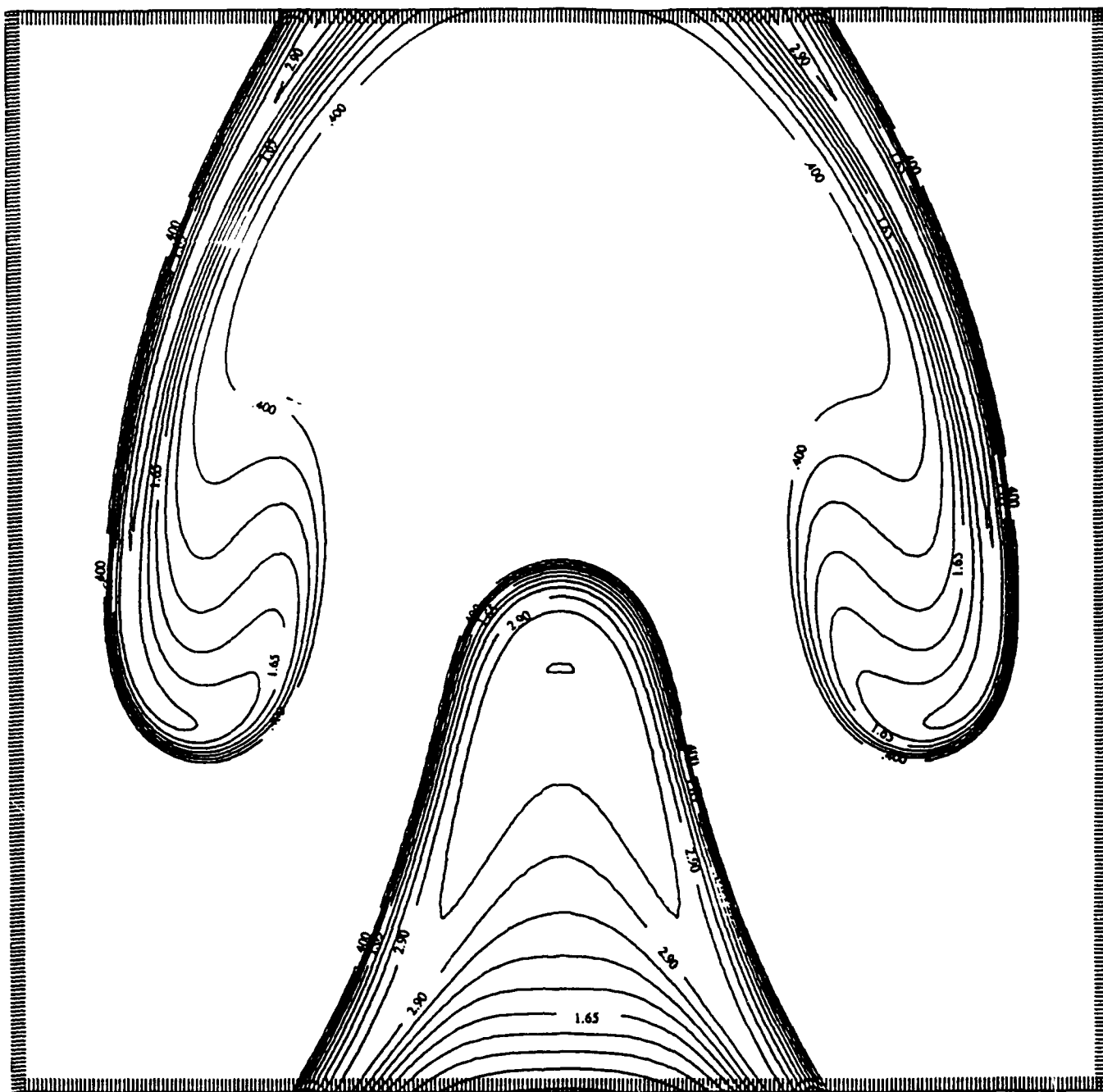


Figure 9a. Density contour at  $t = 4.5$  for the initial data (4.4).



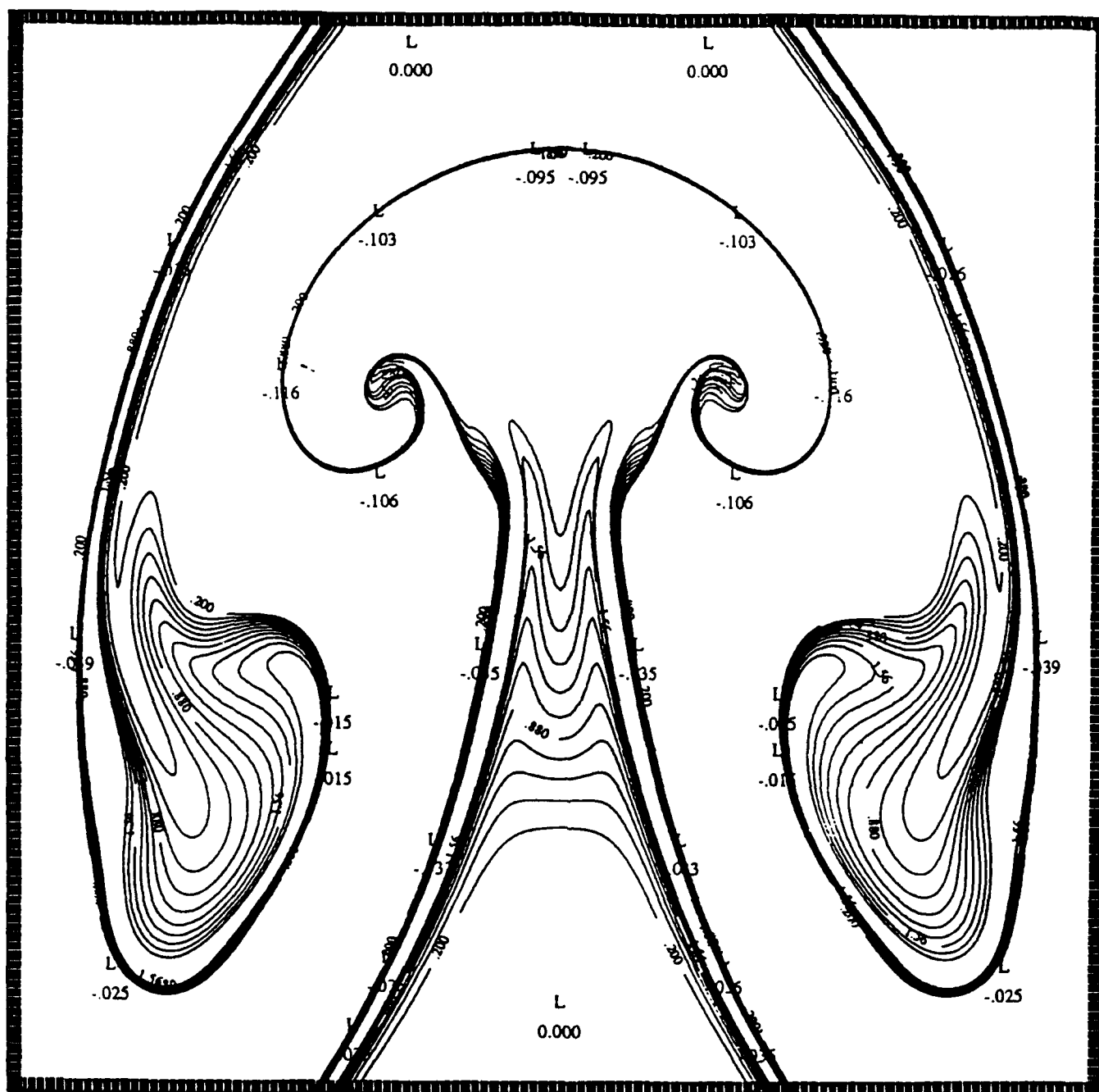


Figure 9b. Density contour at  $t = 1$  for the initial data (4.4).

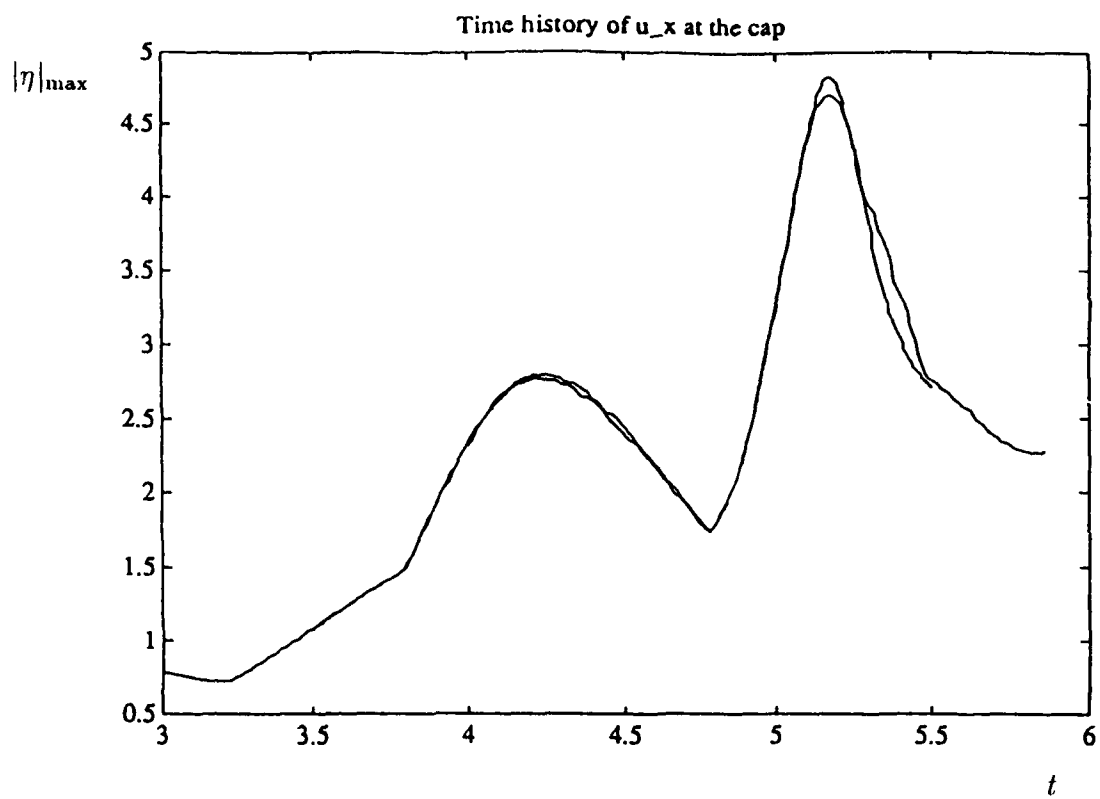


Figure 9c. Time history of the strain rate at the cap.

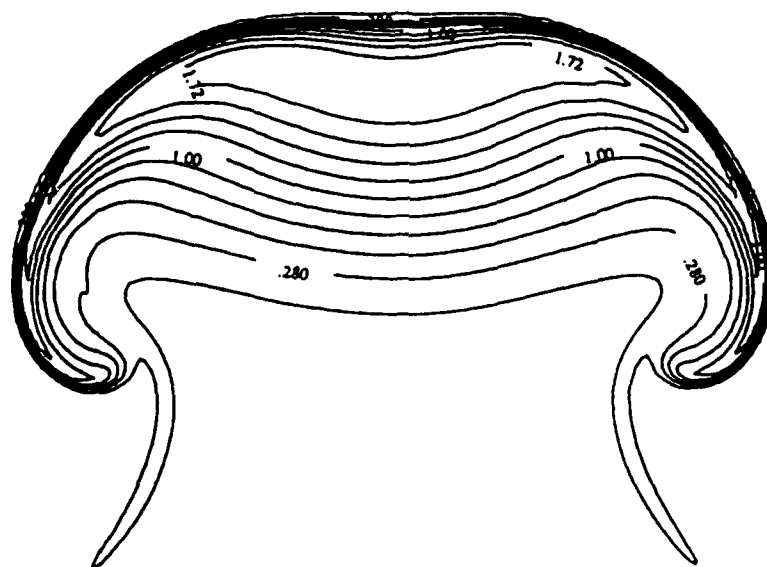


Figure 10a. Density contour at  $t = 3.5$  for another set of initial data.

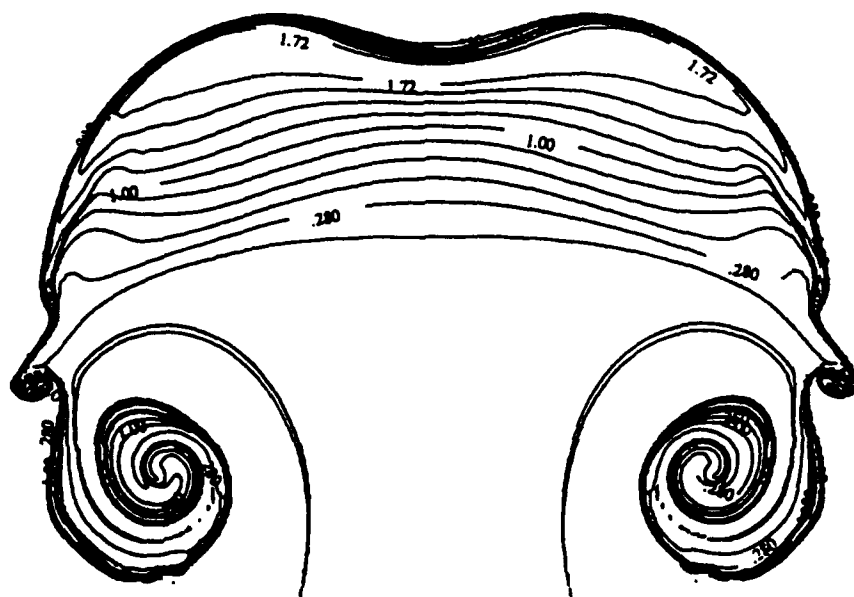


Figure 10b. Density contour at  $t = 5$  for the same data.

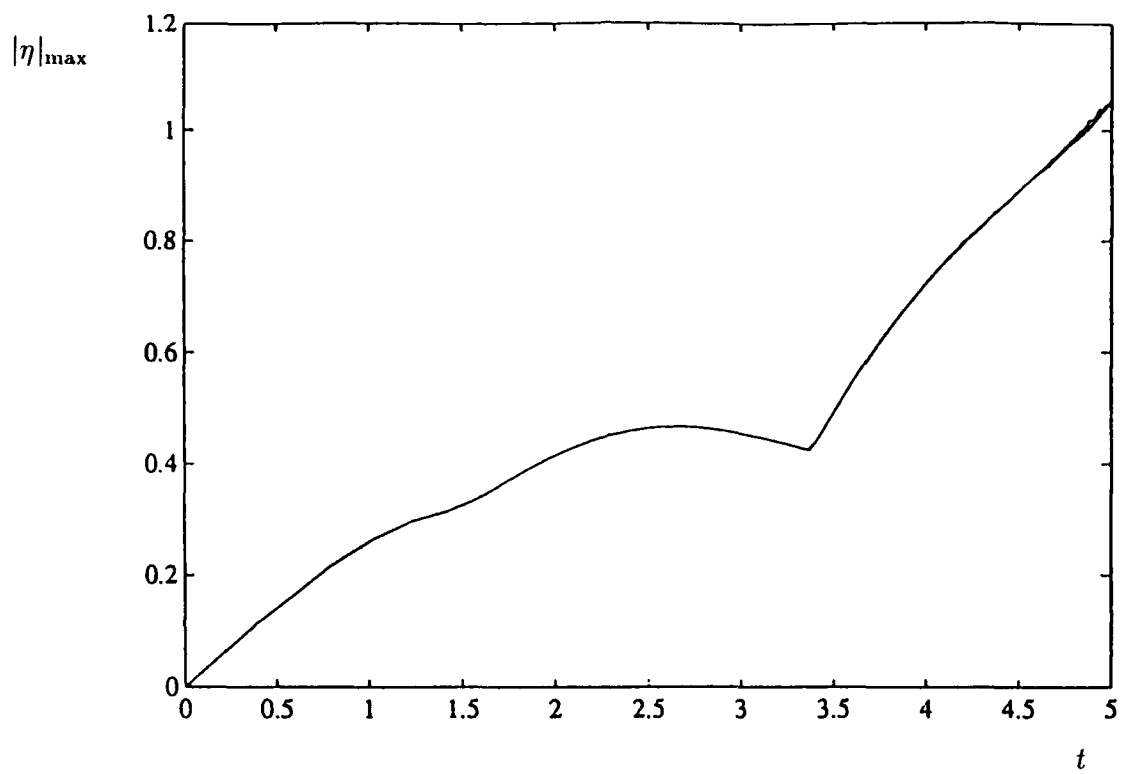


Figure 10c. Time history of the strain rate at the cap.



Figure 11. Contour plot of density in another set of calculation.

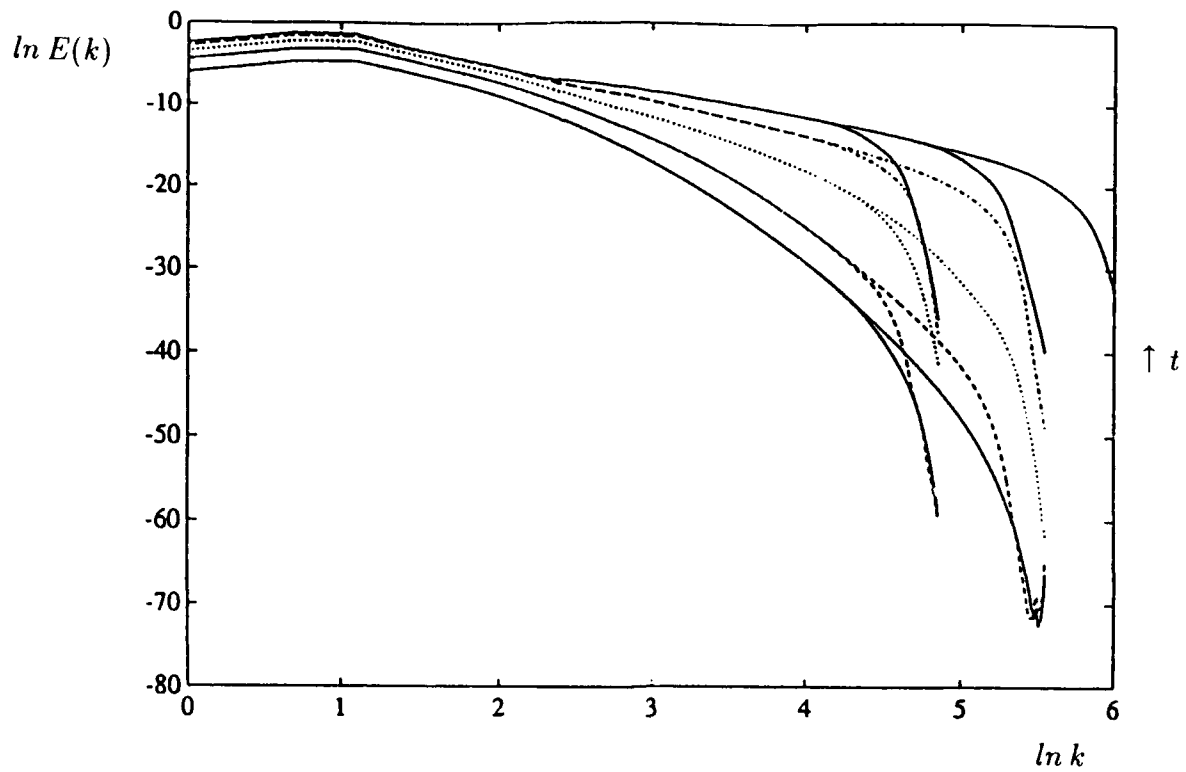


Figure 12. Evolution of energy spectrum for the initial data (4.1) at times:  $t=0.5$ , 1, 1.5, 2, and 2.5 calculated using SP10 on the grids:  $256^2$ ,  $512^2$  and  $1024^2$ . Only the spectrum at  $t=2.5$  is shown for the calculation on the  $1024^2$  grid..

REPORT DOCUMENTATION PAGE			Form Approved OMB No 0704-0188	
<small>Public reporting burden for this collection of information is estimated to average 1 hour per response, including the time for reviewing instructions, searching existing data sources, gathering and maintaining the data needed, and completing and reviewing the collection of information. Send comments regarding this burden estimate or any other aspect of this collection of information, including suggestions for reducing this burden, to Washington Headquarters Services, Directorate for Information Operations and Reports, 1215 Jefferson Davis Highway, Suite 1204, Arlington, VA 22202-4302, and to the Office of Management and Budget, Paperwork Reduction Project (0704-0188), Washington, DC 20503.</small>				
1. AGENCY USE ONLY (Leave blank)		2. REPORT DATE August 1992		3. REPORT TYPE AND DATES COVERED Contractor Report
4. TITLE AND SUBTITLE NUMERICAL STUDY OF THE SMALL SCALE STRUCTURES IN BOUSSINESQ CONVECTION			5. FUNDING NUMBERS C NAS1-18605 C NAS1-19480	
6. AUTHOR(S) Weinan E Chi-Wang Shu			WU 505-90-52-01	
7. PERFORMING ORGANIZATION NAME(S) AND ADDRESS(ES) Institute for Computer Applications in Science and Engineering Mail Stop 132C, NASA Langley Research Center Hampton, VA 23665-5225			8. PERFORMING ORGANIZATION REPORT NUMBER ICASE Report No. 92-40	
9. SPONSORING / MONITORING AGENCY NAME(S) AND ADDRESS(ES) National Aeronautics and Space Administration Langley Research Center Hampton, VA 23665-5225			10. SPONSORING / MONITORING AGENCY REPORT NUMBER NASA CR-i89695 ICASE Report No. 92-40	
11. SUPPLEMENTARY NOTES Langley Technical Monitor: Michael F. Card Final Report Submitted to Physics of Fluids A				
12a. DISTRIBUTION AVAILABILITY STATEMENT Unclassified - Unlimited  Subject Category 64,67			12b. DISTRIBUTION CODE	
13. ABSTRACT (Maximum 200 words) Two-dimensional Boussinesq convection is studied numerically using two different methods: a filtered pseudospectral method and a high order accurate ENO scheme. The issue whether finite time singularity occurs for initially smooth flows is investigated. The numerical results suggest that the collapse of the bubble cap reported by Pumir and Siggia is unlikely to occur in resolved calculations. The strain rate corresponding to the intensification of the density gradient across the front saturates at the bubble cap. We also found that the cascade of energy to small scales is dominated by the formulation of thin and sharp fronts across which density jumps.				
14. SUBJECT TERMS Boussinesq convection; singularities; spectral method; ENO scheme			15. NUMBER OF PAGES 22	
			16. PRICE CODE A03	
17. SECURITY CLASSIFICATION OF REPORT Unclassified	18. SECURITY CLASSIFICATION OF THIS PAGE Unclassified	19. SECURITY CLASSIFICATION OF ABSTRACT	20. LIMITATION OF ABSTRACT	